




Article

Synthesis, Optical and Electrical Characterization of Amino-alcohol Based Sol-gel Hybrid Materials

Bárbara R. Gomes, Rita B. Figueira * , Susana P. G. Costa , M. Manuela M. Raposo 
and Carlos J. R. Silva † 

Centro de Química, Universidade do Minho, Campus de Gualtar, 4710-057 Braga, Portugal;
barbara.sgomes11@gmail.com (B.R.G.); spc@quimica.uminho.pt (S.P.G.C.);
mfox@quimica.uminho.pt (M.M.M.R.)

* Correspondence: rbacelarfigueira@quimica.uminho.pt or rita@figueira.pt

† This paper is dedicated to the memory of Professor C. J. R. Silva who passed away suddenly on 27 August 2020.

Received: 22 October 2020; Accepted: 10 November 2020; Published: 12 November 2020



Abstract: This manuscript describes the synthesis and characterization of five new organic–inorganic hybrid (OIH) sol-gel materials that were obtained from a functionalized siloxane 3-glycidoxypropyltrimethoxysilane (GPTMS) by the reaction with the new Jeffamine[®], namely three different diamines, i.e., EDR-148, RFD-270, and THF-170, a secondary diamine, i.e., SD-2001, and a triamine, i.e., T-403. The OIH sol-gel materials were characterized by UV-visible absorption spectrophotometry, steady-state photoluminescence spectroscopy, and electrochemical impedance spectroscopy. The reported OIH sol-gel materials showed that, with the exception of the samples prepared with Jeffamine[®] SD-2001, the transmittance values ranged between 61% and 79%. Regarding the capacitance data, the values reported changed between 0.008 and 0.013 nF cm⁻². Due to their optical and electrical properties these new OIH materials show promising properties for applications as support films in an optical sensor area such as fiber sensor devices. Studies to assess the chemical stability of the OIH materials in contact with cement pastes after 7, 14, and 28 days were also performed. The samples prepared with THF-170 and GPTMS, when compared to the samples prepared with RFD-270 and T-403, exhibited improved behavior in the cement paste (alkaline environment), showing promising properties for application as support film in optical fiber sensors in the civil engineering field.

Keywords: hybrids; sol-gel; materials; amino-alcohol

1. Introduction

In the last few decades, the design and development of organic–inorganic hybrid (OIH) sol-gel materials for a wide range of applications has achieved a high scientific proficiency level. Several OIH materials have been reported for applications such as coatings for corrosion mitigation, smart windows, photochromic and electrochromic materials, sensors, optical filters, and absorbers, among others. The sol-gel method is recognized as a green, low-cost, and versatile route that allows organic–inorganic hybrid (OIH) materials to be obtained in a simple way by the reaction between polyetheramines and organoalkoxysilanes. The most remarkable properties of such OIH materials include chemical stability, suitable dielectric properties, selective ion binding, and ion conducting ability, depending on their organic and inorganic components. Such materials have also been reported as interesting luminescent sources [1–5] and hosts of luminescent species [6–13]. For instance, Severo Rodembusch et al. reported for the first time the synthesis of fluorescent hybrid aerogels in the blue–green–yellow region. The dyes were obtained by the reaction of amino benzazole derivatives with 3-(triethoxysilyl)propyl isocyanate.

As precursor a pre-polymerized tetraethoxysilane was used [8]. In 2015, Brito et al. reported the entrapment of blue–green luminescent C-dots in transparent silica. The silica was obtained by pyrolysis of the methyl groups present in the nanometric silica grains [12].

Other materials such as siloxane-polyether OIH materials, also known as di- or tri-ureasil, have also been widely reported [11,14–26] for an extensive range of applications. The most common strategy to prepare such materials with the sol-gel method involves several hydrolysis and polycondensation reactions allowing their morphology, structure, and chemical composition to be tuned. For instance, Boev et al. [15] reported a simple procedure for the synthesis of ureasilicate materials. The authors studied the influence of the molar ratio between 3-isocyanate propyltriethoxysilane (ICPTES) and Jeffamine[®] ED-600. A homogeneous and flexible material was attained and it was concluded that by changing the catalyst nature and the molar ratio of ICPTES/Jeffamine[®] highly transparent samples within the visible range with dissimilar elastic properties were obtained. Later, the studied materials were doped with different nanoparticles, including CdS [16,26–28], CdSe [20,29], Zn_xCd_{1-x}S [17], and PbS [30]. Ureasilicate materials have also been reported as coatings for corrosion mitigation in alkaline environments [19,22,31] and in the presence of chloride ions [32,33], showing good performance for the desired purpose. These materials were also reported as films for the development of a relative humidity (RH) optical fiber sensor [23]. The ureasilicate material was deposited by dip coating the fiber and studied in the range of 5% to 95% of RH. It was also concluded that when compared to other polymer-based solutions, the proposed material showed enhanced durability and sensitivity (22.2 pm/% RH) in monitoring the RH of two concrete blocks for one year [23]. Willis-Fox et al. [34] reported a strategy for the preparation of a conjugated polymer-di-ureasil composite material showing a tunable emission color from blue to yellow using a simple sol-gel method. Moreira et al. [18] reported the synthesis of ureasilicates and amino-alcohol silicate OIH sol-gel materials. The amino-alcohol silicates were obtained by reacting Jeffamine[®] ED-600 or Jeffamine[®] ED-900 with 3-glycidoxypropyltrimethoxysilane (GPTMS) using a molar ratio of GPTMS:Jeffamine[®] = 2:1. The GPTMS precursor is a suitable molecule establishing amino-alcohol bonds between the inorganic (silicate) and organic (Jeffamine) components (i.e., a polyether chain) similar to that reported for the ureasilicate matrix [18]. The authors obtained flexible xerogels with high transparency within the visible range and showed that the amino-alcohol silicate samples exhibited suitable optical and mechanical properties that can lead to the production of low-cost and variable shape diffraction lenses in a wide range of substrates for optical applications [18]. Figueira et al. also reported the use of amino-alcohol silicate matrices as coating materials for corrosion mitigation of galvanized steel in an alkaline environment [22,35].

In the last few decades the use of optical fiber sensors (OFS) to monitor physical parameters of structures in the civil engineering field has been widely employed. For instance, the application of OFS to monitor properties such as the curvature and deflection of bridges [36–39], the onset of cracking [40–42], and temperature [43,44] has been consistently reported. Nevertheless, besides physical properties, other parameters such as pH level [45,46], relative humidity [47–49], chloride content [50–52], and alkali-silica reactions (ASR) [53] are also responsible for earlier failure of civil engineering structures. The development of robust and accurate monitoring sensing systems is of extreme importance as they will allow the service life of concrete structures to increase and costs saved at the same time. The monitoring of concrete structures using functionalized optical fiber sensors (OFS) with sol-gel films revealed to be an interesting approach to increase its service life [54].

Considering the steadily increasing attention being paid to these OIH films together with their promising properties, further research is needed. Therefore, this work reports the synthesis and optical and electrochemical characterization of new OIH amino-alcohol silicate-based materials for potential application on an OFS for health monitoring of concrete structures. In this manuscript, the new Jeffamines[®] will be considered. To the authors' knowledge no studies using the Jeffamine[®] EDR-148, Jeffamine[®] RFD-270, Jeffamine[®] THF-170, Jeffamine[®] SD-2001, and Jeffamine[®] T-403 have been reported. Therefore, three different diamines (Jeffamine[®] EDR-148, Jeffamine[®] RFD-270,

and Jeffamine[®] THF-170), a secondary diamine (Jeffamine[®] SD-2001), and a triamine (Jeffamine[®] T-403) were made to react with GPTMS-producing amino-alcohol silicate matrices. More specifically, five new different OIH sol-gel materials were synthesized.

To the authors' knowledge no studies have been reported on the synthesis of OIH xerogel films using GPTMS and Jeffamine[®] EDR-148, Jeffamine[®] RFD-270, or Jeffamine[®] THF-170 as a siloxane precursor. Concerning Jeffamine[®] T-403, this precursor has been reported by different authors for a wide range of applications [55–59]. For instance, Spírkpová et al. in 2003 reported the synthesis and structural and mechanical properties of the OIHs obtained by the reaction between GPTMS and three different Jeffamines[®]: T-403, D-230, and D-400 [55]. Nevertheless, the authors used different ratios and synthesis parameters [55].

The OIH sol-gel materials synthesized were characterized by UV–visible spectrophotometry, steady-state photoluminescence spectroscopy, and electrochemical impedance spectroscopy. The reported OIH sol-gel materials show interesting optical properties for application as a support matrix in OFS and the capacitance values changed between 0.008 and 0.013 nF cm⁻². Preliminary studies were also conducted to assess the chemical stability of the OIH materials in contact with cement pastes for 7, 14, and 28 days. The samples prepared with Jeffamine[®] THF-170 and GPTMS, when compared to the others, exhibited improved and promising properties in a cement paste environment.

2. Experimental

2.1. Reagents

Figure 1 shows the structure and acronym (in bold) of the precursors used in the synthesis of the OIH sol-gel materials. The structure of Jeffamine[®] THF-170 (*Poly(oxy-1,4-butanediyl), α -hydro- Ω -hydroxy-,polymer with ammonia*) (Huntsman Corporation, Pamplona, Spain), hereafter referred to as THF-170, was not provided by the supplier. The structure which is indicated in Figure 1 is based on the information reported by Létoffé et al. for a similar Jeffamine[®] (Jeffamine[®] THF-100) [60]. Five different Jeffamines[®] (structurally identified as polyetheramines) were kindly supplied by Huntsman, with different molecular weights and reactivity. Jeffamine[®] EDR-148 is the most reactive Jeffamine[®] when compared to diamines and triamines due to the unhindered nature of the amine groups (vide Figure 1).

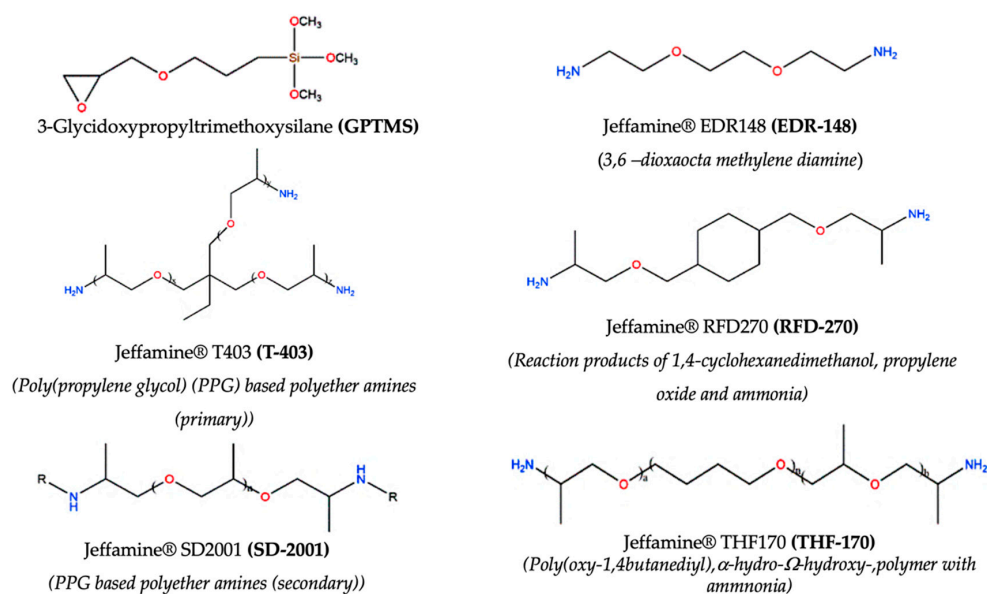


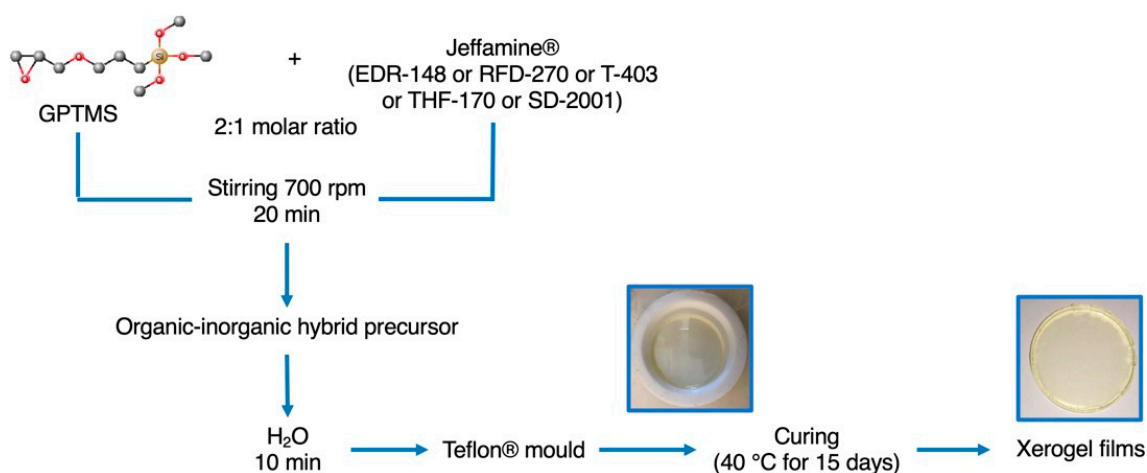
Figure 1. Structure and acronym (in bold) of the precursors used in the synthesis of the organic–inorganic hybrid sol-gel materials.

Jeffamine[®] RFD-270 is an amine containing both rigid (cycloaliphatic) and flexible (etheramine) moieties in the same molecule and the acronym RFD stands for “rigiflex diamine” (vide Figure 1). Jeffamine[®] T-403 is a triamine prepared by the reaction of propylene oxide with a triol initiator, followed by the amination of the terminal hydroxyl groups (vide Figure 1). The Jeffamine[®] THF-170 is based on a poly(tetramethylene ether glycol)/(poly(propylene glycol) copolymer. Jeffamine[®] SD-2001 is a polyetheramine, where SD stands for “secondary diamine.” The secondary amine groups provide a much slower reaction compared to primary amine groups.

All the precursors used, namely the Jeffamines[®] and the GPTMS (97%, Sigma-Aldrich, St. Louis, MO, USA), were used as supplied. As solvents, tetrahydrofuran (99.5% stabilized with ~ 300 ppm of BHT, Panreac, Darmstadt, Germany) and ultra-pure water with high resistivity (higher than 18 MΩ cm) obtained from a Millipore water purification system (Milli-Q[®], Merck KGaA, Darmstadt, Germany) were employed.

2.2. Synthesis Procedure of Xerogel Films

The obtained xerogel films were synthesized in sequential steps, as schematized in Scheme 1.



Scheme 1. Main steps involved in the synthesis of the OIH sol-gel matrices.

Before the 3-glycidoxypropyltrimethoxysilane (GPTMS) addition, the Jeffamines[®] were solubilized using tetrahydrofuran. After 10 min, the GPTMS was added to the Jeffamine[®] (EDR-148, RFD-270, T-403, THF-170, or SD-2001) using a molar ratio of 2 GPTMS:1 Jeffamine[®] in a glass vessel under stirring at 700 rpm for 20 min, with the exception of Jeffamine[®] RFD-270, which was prepared with a molar ratio of 1 GPTMS:1 Jeffamine[®].

The reaction between the amine end group ($-NH_2$) of the Jeffamine[®] with different molecular weight and structure (Jeffamine[®] EDR-148, Jeffamine[®] RFD-270, Jeffamine[®] T-403, Jeffamine[®] THF-170, and Jeffamine[®] SD-2001) and the epoxy group of GPTMS led to the formation of the OIH precursors of the future gel matrices that are named as conventional amino-alcohol silicates and referred to as A(148), A(270), A(403), A(170), and A(2001). The numbers in parentheses stand for the Jeffamine[®] used, with the reference names indicated in Figure 1. The second step included the addition of H₂O to obtain an H₂O:Jeffamine[®] molar ratio equal to 5.94. The mixture was stirred for another 10 min and placed into a Teflon[®] mold (DuPont, Wilmington, DE, USA) and sealed with Parafilm[®] that was pin-holed and placed in an oven (UNB 200, Memmert, Buechenbach, Germany) and kept at 40 °C for 15 days. This procedure ensures precise control and reproducibility of the conditions of hydrolysis/condensation reactions as well as the evaporation of the residual solvents. Scheme 1 shows that the implemented preparation conditions applied allowed homogeneous and transparent film samples free of cracks to be obtained.

2.3. OIH Sol-Gel Film Characterization

The OIH materials synthesized were characterized optically and electrochemically. All the measurements were conducted at room temperature. The UV-visible transmission and absorption spectra of the OIH film samples were obtained using a spectrophotometer (UV-2501 PC, Shimadzu, Duisburg, Germany) in the range of 250–700 nm. The fluorescence spectra were obtained using a spectrofluorometer (Fluoromax-4, Horiba Jovin Yvon, Madrid, Spain). The emission spectra were recorded in the wavelength range of 300–700 nm using different excitation wavelengths and acquired at front-face geometry at room temperature.

Electrochemical impedance spectroscopy (EIS) measurements were carried out to characterize resistance, electrical conductivity, and the electric permittivity of the prepared OIH films. Measurements were performed using a two-electrode system in which the film was placed between two parallel Au disc electrodes (10 mm diameter and 250 μm thickness) and a support cell [33]. Measurements were performed in a Faraday cage using a potentiostat/galvanostat/ZRA (Reference 600+, Gamry Instruments, Warminster, PA, USA) by applying a 10 mV (peak-to-peak, sinusoidal) electrical potential within a frequency range from 1×10^5 Hz to 0.01 Hz (10 points per decade) at open circuit potential. The frequency response data were displayed in a Nyquist plot. The Gamry ESA410 Data Acquisition software was used for data fitting purposes.

2.4. Preparation of Cement Paste

The chemical stability of the different OIH films was studied in a cement paste. The cement paste was prepared using cement type I 42,5R and distilled water. The ratio of water to cement (w/c) used was equal to 0.5. The OIH films used were 10 mm in diameter and the thickness ranged between 1.4 and 1.8 mm.

3. Results and Discussion

3.1. UV-Visible Spectrophotometry Analysis

Figure 2 shows the optical transmittance spectra as a function of wavelength obtained for the synthesized xerogel films A(148), A(270), A(403), A(170), and A(2001). The A(2001) samples show the lowest transmittance, followed by A(148), A(170), A(270), and A(403), with A(403) showing the highest transmittance values of between 400 and 700 nm.

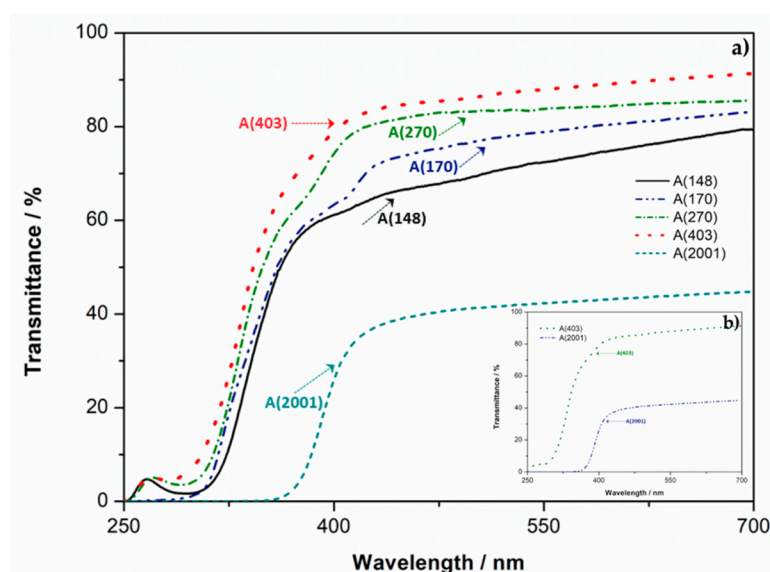


Figure 2. UV-visible transmission spectra obtained for xerogel films (a) A(148), A(270), A(403), A(170), and A(2001) and as an inset detail of (b) A(403) and A(2001).

In the UV region between 250 and 300 nm, all the samples showed low transmittance, which is in accordance with the literature [18]. The transmittance data shows that at 400 nm wavelength, the xerogel that provided the highest value was A(403) with around 79%. At the same wavelength, A(270) showed a transmittance of around 74% and the lowest transmittance was given by A(2001) with a value of around 26%. At 400 nm, A(148) and A(170) showed a transmittance of 61% and 63%, respectively. As the wavelength increases the transmittance values increase, with A(403) reaching the highest value, i.e., 89% at 600 nm.

These results are in agreement with the results reported by Moreira et al. [18] and by Erdem et al. [61]. Both authors reported that the OIHs obtained with lower molecular weights show higher transmittance than films prepared with higher molecular weights. Moreira et al. [18] described the reaction between Jeffamine[®] ED-600 and GPTMS as showing higher transmittance than films prepared by the reaction between Jeffamine[®] ED-900 and GPTMS. This behavior suggests that the OIH transmittance is related to the molecular weight of the Jeffamine[®]. Another explanation may be related to the structure involved together with the interactions established between the Jeffamine[®] and the GPTMS. Zea Bermudez et al. reported a study focused on the synthesis and FTIR characterization of OIHs using as precursors Jeffamines[®] ED-600, ED-900, and ED-2000 with 3-isocyanatepropyltriethoxysilane. It was reported that the FTIR spectrum of U(2000) showed that the polyether chains of the parent diamine become less ordered upon incorporation into the inorganic backbone. The number of oxyethylene units present affected the amide I and amide II bands. This indicated that the N–H groups of the urea linkage were involved in the hydrogen bonds of different strengths. Moreover, the authors proposed the existence of non-hydrogen-bonded urea groups and hydrogen-bonded urea–urea and urea–polyether associations. On one hand the formation of urea–urea structures was favored in the U(600), while on the other hand the number of free carbonyl groups was higher in U(2000) [14]. Similar behavior for the A(2001) may be expected, which may justify the huge difference of transmittance between A(148), A(170), A(270), and A(403) since Jeffamine[®] SD-2001 is a difunctional secondary amine derived from Jeffamine[®] ED-2000. Nevertheless, since in this case GPTMS was used instead of 3-isocyanatepropyltriethoxysilane no further conclusions can be drawn. Therefore, further studies, namely FTIR analysis, should be conducted in order to clarify the interactions between the precursors.

The thickness of the films ranged between 0.913 mm and 1.434 mm. The thickness obtained for the OIHs for A(148), A(270), A(403), A(170), and A(2001) was 1.301 mm, 0.913 mm, 1.051 mm, 1.434 mm, and 1.024 mm, respectively. Therefore, the absorbance measurements were divided by the thickness obtained for each film. Figure 3 shows the UV-vis absorption spectra normalized to the film thickness of the four synthesized xerogel films (A(148), A(270), A(403), A(170), and A(2001)).

The highest absorbance peaks were found in the UV region between 250 and 300 nm (Figure 3). The maximum absorption wavelength obtained for each xerogel film for A(148), A(270), A(403), A(170), and A(2001) was 294 nm, 290 nm, 281 nm, 276 nm, and 310 nm, respectively. Regardless of the structure of the Jeffamine[®] used, as the molecular weight of Jeffamine[®] increases, the maximum wavelength in the UV region (between 250–300 nm) decreases. An exception was found for A(2001), which showed the highest molecular weight and a maximum at a wavelength of around 310 nm. The highest and the lowest absorbance peaks were obtained for A(2001) and A(403) xerogel films. Figure 3 also shows that, with the exception of A(2001), all the other OIH matrices are transparent from 300 nm forward. Therefore, these materials are suitable for probe immobilization in the range between 300 and 700 nm. Considering the low transmittance obtained for A(2001) and its translucency, no further studies were conducted in characterizing A(2001). Moreover, previous studies showed that as the molecular weight of a Jeffamine[®] increases, the resistance of the OIHs to a highly alkaline environment decreases [22,32].

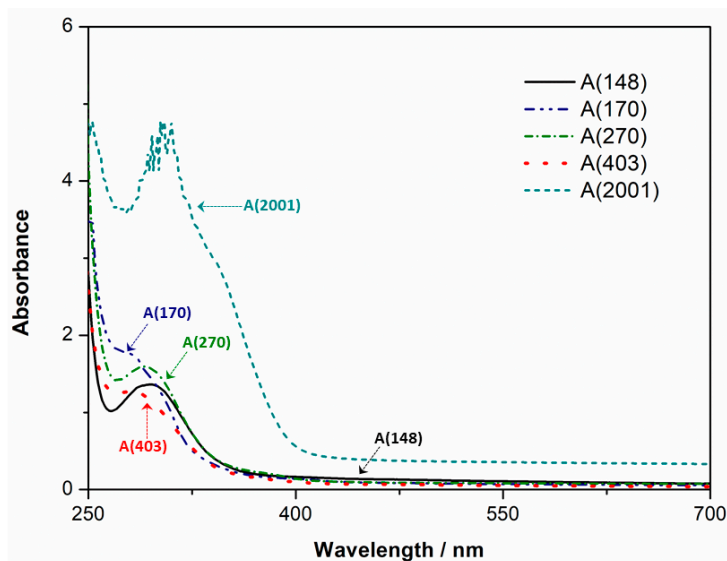


Figure 3. UV-visible absorption spectra normalized for the thickness of each xerogel film, namely A(148), A(270), A(403), A(170), and A(2001).

3.2. Photoluminescence Spectrophotometry Analysis

Figure 4 shows the emission fluorescence spectra obtained for the synthesized xerogel films A(148), A(270), A(403), and A(170) at different excitation wavelengths. The limits of excitation wavelengths were defined according to the maximum wavelength recorded for each OIH film in UV-vis analysis, always starting at 250 nm.

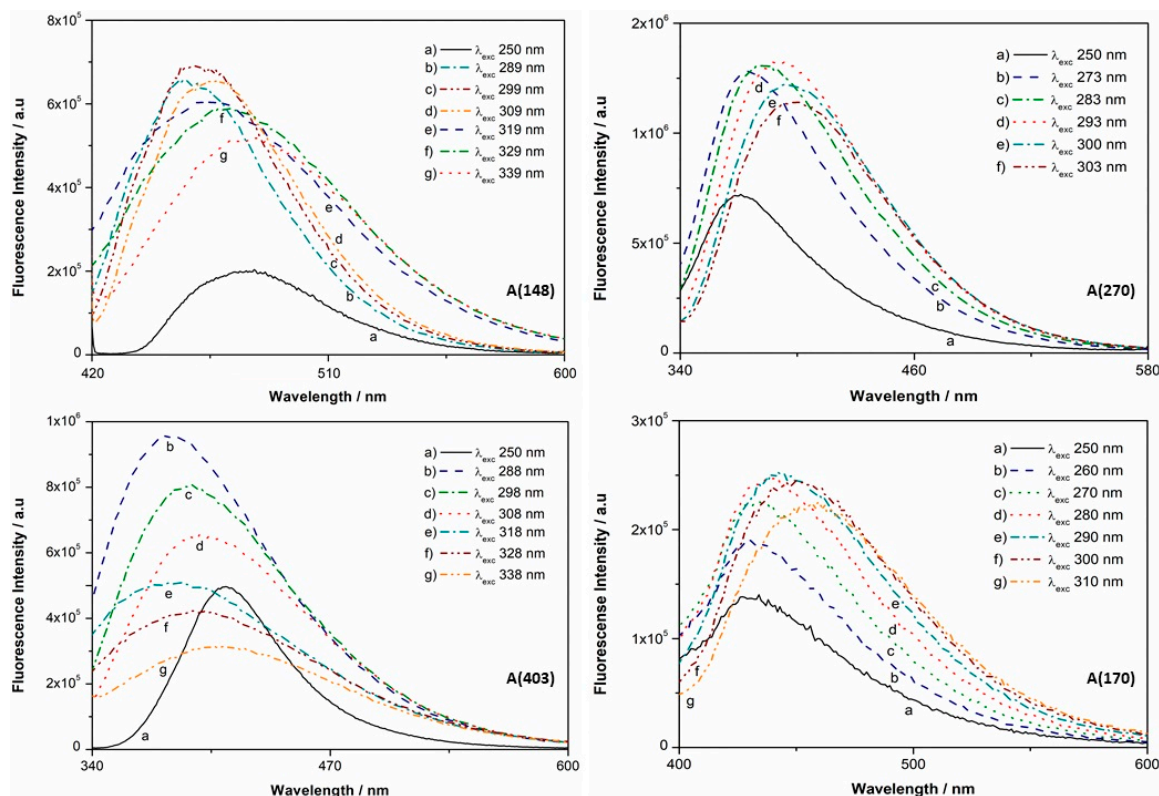


Figure 4. Photoluminescence spectra obtained for xerogel films A(148), A(270), A(403), and A(170).

Figure 4 shows that the OIH materials show an intrinsic emission. In the case of the A(270) and A(170) OIH matrices, it can be observed that the wavelength of the emission peak displaces to higher wavelengths when the excitation wavelength increases. This intrinsic emission linked to these OIH matrices is due to the photoinduced proton transfer between defects $\text{NH}_3^+/\text{NH}^-$ and due to the electron–hole recombination occurring in the siloxane nanoclusters [62]. The emission wavelength dependency with the excitation energy is connected to unorganized processes that are generally linked to transitions that occur between localized states in non-crystalline structures [62]. According to Carlos et al. [2], in OIHs similar to the ones reported here the hierarchy in the silica backbone dimension defines the emission wavelength. This is in agreement with the findings reported here. This energy dependence of the emission wavelength with the excitation energy is related to the size of the silica clusters [63]. The same authors reported that larger clusters emit at longer wavelengths than smaller clusters. Generally, shorter polyether chains (A(148) and A(403)) provide samples with higher photoluminescence while larger chains may induce a dilution effect that may reduce the luminescence efficiency [63], which is in agreement with the data reported here. In the case of A(148) and A(403) it can be observed that the wavelength of the emission peak displaces to lower wavelengths when the excitation wavelength increases. Photoluminescence spectra of the samples with shorter polymer chains such as the ones used in A(148) and A(403) suggest that the electron–hole recombination occurring in the siloxane nanoclusters is large enough to allow efficient energy-transfer mechanisms.

The full width at half maximum did not decrease with decreasing excitation energy. Considering that the OIH materials are a biphasic system (i.e., organic and inorganic components are mixed at nanometric scale), this may contribute to a higher light scattering that may lead to changes within the sample and to a general broadening of the peaks. Generally, Figure 4 shows that the full width at half maximum did not decrease with decreasing excitation energy.

Figure 5 shows the photographs of the xerogel samples synthesized and their photoluminescence response when excited with UV light, i.e., an excitation wavelength of 365 nm.

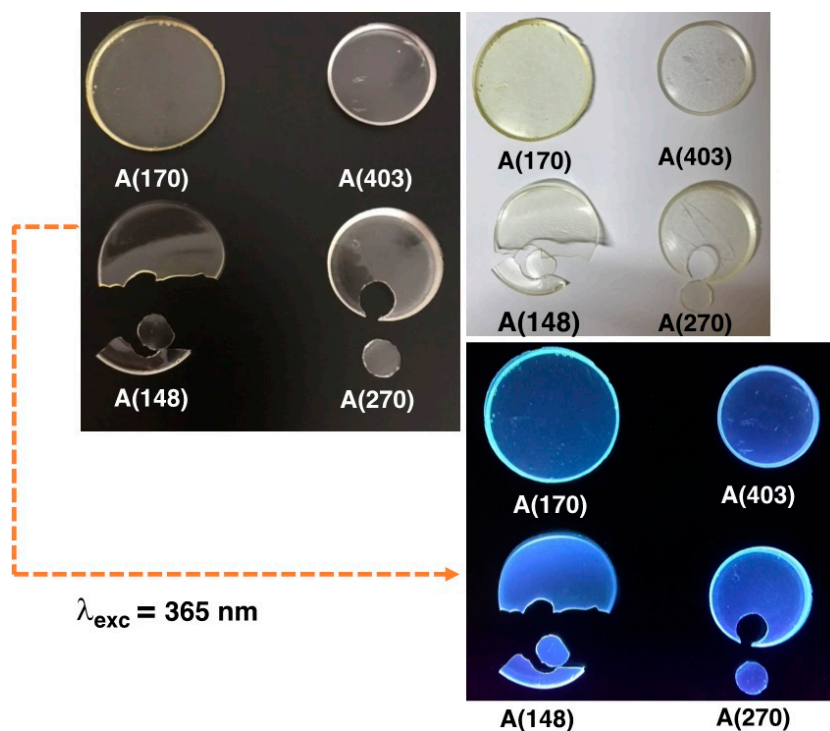


Figure 5. Amino-alcohol silicate samples and their photoluminescence response after an excitation with a light with a wavelength of 365 nm.

The blue color of the A(148), A(270), A(403), and A(170) xerogels after excitation with UV radiation arises from the photoluminescence emission in the 450–470 nm region [29]. It is generally accepted that silicon-based materials can emit light within a wide energy region that ranges from ultraviolet to infrared [2,64,65]. The backbone silicon-based structures are responsible for the emission energy, i.e., an increase in the siliceous network may result in a decrease in the corresponding energy gap [2]. The emission energy of silicon-based materials depends on the hierarchy of their backbone dimensions. Since the network dimension changes, the band gap energies change accordingly. This dependence of the energy gap on the backbone dimensions is related to the extension of the silicon σ -conjugations through the OIH network. These induce the delocalization of the electrons, leading to the formation of electronic band structures. Increasing their extension along the silicon backbone induces a decrease in the energy gap values, with a corresponding increase in the skeleton dimensions. Moreover, the Si–O–Si network is considered responsible for the blue emission of oxidized porous silicon [2].

3.3. EIS Measurements

Electrochemical impedance spectroscopy (EIS) is a very interesting technique widely used for the characterization of OIH sol-gel materials [32,33,35,66,67]. Figure 6 shows the Nyquist plots of the pure OIH films based on A(270) (Figure 6a), A(403) (Figure 6b), A(2001) (Figure 6c), and A(170) (Figure 6d) matrices, correspondingly. The experimental and the fitting results are shown in the Nyquist plots (Figure 6) and are schematized by squares and a continuous line, respectively. The equivalent electrical circuits (EEC) used for each sample were introduced as an inset in each Nyquist plot.

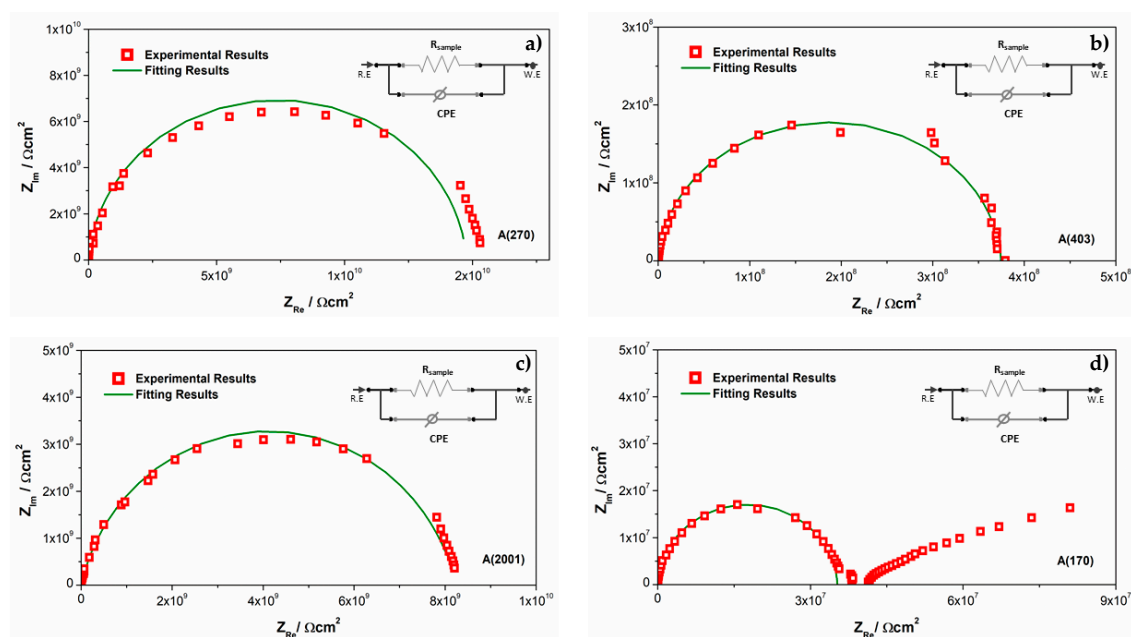


Figure 6. Complex plane impedance plots obtained for the OIH films based on: (a) A(270); (b) A(403); (c) A(2001); and (d) A(170) matrices (inset displayed in the EEC (equivalent electrical circuit) diagram adapted for fitting purposes).

The Nyquist plots illustrated in Figure 6 show that generally in the region of high frequencies a semicircle intersects the x-axis. It can also be observed that the diameter of the semicircle changes with the Jeffamine[®] used. This indicates that the dielectric properties of the OIH sol-gel materials (e.g., conductivity, capacitance, etc.) change with the different Jeffamine[®] used in the OIH synthesis. The data obtained at lower frequencies (Figure 6d) describes a line suggesting another electrochemical process that can be assigned to the interfacial phenomena between the gold electrodes and the OIH disc, which is in accordance with the literature [35]. However, this particular phenomenon will not be considered in the EIS analysis since it is not necessary to characterize the dielectric properties of the

materials that are being studied. The EIS results regarding OIH A(148) films are not reported since it was not possible to perform its measurements. This may be due to the high rigidity and the difficulty in establishing the contact between the gold electrodes and the A(148) OIH discs. The high rigidity contributes to a poor electric contact between the OIH film and the gold electrode discs, disabling the electrical response.

The Nyquist plots (Figure 6) show a depressed form, therefore the analysis of all the impedance responses was based on an EEC where constant phase elements (CPE) were used in place of pure capacitance.

As reported, the impedance of a CPE can be defined as [68]:

$$Z_{\text{CPE}} = \frac{1}{[Q(j\omega)^\alpha]} \quad (1)$$

In Equation (1), both Q and α parameters are independent of the frequency. When $\alpha = 1$, Q stands for the capacity of the interface [67]. However, when $0 < \alpha < 1$ the system shows behavior that is generally linked to surface heterogeneity and the impedance for the EEC is given by Equation (2) [68]:

$$Z_{\text{CPE}} = \frac{R_{\text{sample}}}{[1 + (j\omega)^\alpha QR_{\text{sample}}]} \quad (2)$$

The interfacial capacitance (C_{eff}) is given by Equation (3) using the estimated Q value [68]:

$$C_{\text{eff}} = [QR_{\text{sample}}^{(1-\alpha)}]^\frac{1}{\alpha} \quad (3)$$

Table 1 shows the values of the proposed EEC elements obtained from the EIS data fitting for all the OIH materials synthesized.

Table 1. Values of elements of the proposed EEC obtained from EIS data fitting of the OIH materials synthesized and errors in percentage. For comparison purposes the data reported for A(400) [35], A(900) [35], and A(2000) [35] were also included.

OIH Sample	$R_{\text{Sample}} (\Omega)$	CPE (Q) ($\text{S}^\alpha \Omega^{-1}$)	α	χ^2
A(270)	4.58×10^{10} (± 0.83 %)	6.75×10^{-12} . (± 1.63 %)	0.96	3.31×10^{-3}
A(400) [35]	8.53×10^8 (± 0.60 %)	7.38×10^{-11} ($\pm 3.65\%$)	0.73 [35]	NR
A(403)	4.67×10^8 (± 0.80 %)	8.23×10^{-12} . (± 2.96 %)	0.97	4.08×10^{-4}
A(900) [35]	5.79×10^4 (± 0.19 %)	4.20×10^{-10} ($\pm 4.34\%$)	0.81 [35]	NR
A(170)	3.53×10^7 (± 0.77 %)	4.76×10^{-12} (± 2.29 %)	0.98	3.20×10^{-4}
A(2000) [35]	3.62×10^4 ($\pm 0.24\%$)	2.27×10^{-9} ($\pm 5.09\%$)	0.71	NR
A(2001)	7.54×10^9 (± 0.853 %)	1.50×10^{-11} . (± 1.71 %)	0.86	9.47×10^{-3}

NR—not reported; CPE—constant phase element.

Table 1 shows that all the resistances of the new OIH film samples synthesized, namely A(170), A(270), A(403), and A(2001), are between 10^7 and $10^{10} \Omega$. With the exception of the values obtained for A(400) [35] (vide Table 1), all the new synthesized OIH materials show higher values when compared to the ones already reported for A(900) and A(2000).

The values obtained for the elements of the EEC proposed and reported in Table 1, i.e., the values of resistance (R_{Sample}), the constant phase element (CPE), and α , were used to obtain the C_{eff} using Equation (3). The resistance (R) and capacitance (C) values were normalized to cell geometry dimensions and calculated using Equations (4) and (5), respectively. The conductivity (σ) and relative permittivity (ϵ_r) were also determined using Equations (6) and (7), respectively. The values were obtained using the

equations below, where A_{Au} is the area of the gold electrodes, d_{sample} is the thickness of the analyzed OIH film sample, and ϵ_0 stands for the vacuum permittivity in $nF\text{ cm}^{-1}$:

$$R = R_{sample} \times A_{Au\text{ disc}} \quad (4)$$

$$C = \frac{C_{eff}}{A_{Au\text{ disc}}} \quad (5)$$

$$\sigma = \frac{d_{sample}}{A_{Au\text{ disc}}} / R_{sample} \quad (6)$$

$$\epsilon_r = \frac{C_{eff} \times d_{sample}}{\epsilon_0} \times A_{Au\text{ disc}} \quad (7)$$

The information regarding the electrical properties of the OIH films produced, including normalized resistance (R), capacitance (C), conductivity (σ), and relative permittivity (ϵ_r), is displayed in Table 2.

Table 2. Electrical properties of the OIH samples based on A(X) matrices. For comparison purposes the data reported for A(400) [35], A(600) [35], A(900) [35], and A(2000) [35] were also included.

OIH Sample	Molecular Weight	log R ($\Omega\text{ cm}^2$)	ϵ_r	C ($nF\text{ cm}^{-2}$)	$-\log \sigma$ ($S\text{ cm}^{-1}$)
A(270)	270	10.05 ± 0.02	17.80 ± 1.53	0.008 ± 0.001	10.76 ± 0.02
A(400) [35]	430	8.69 ± 0.10 [35]	26.90 ± 2.36 [35]	0.035 ± 0.002 [35]	9.85 ± 0.06 [35]
A(403)	440	8.48 ± 0.02	12.56 ± 0.12	$0.0086 \pm 8.37 \times 10^{-5}$	9.37 ± 0.02
A(600) [35]	600	5.97 ± 0.34 [35]	n.a. [35]	n.a. [35]	6.39 ± 0.90 [35]
A(900) [35]	900	4.78 ± 0.13 [35]	28.50 ± 4.00 [35]	0.041 ± 0.006 [35]	5.99 ± 0.05 [35]
A(170)	1700	7.03 ± 0.72	8.12 ± 0.03	$0.005 \pm 2.10 \times 10^{-5}$	7.87 ± 0.72
A(2000) [35]	2000	4.78 ± 0.29 [35]	56.75 ± 9.39 [35]	0.051 ± 0.009 [35]	5.89 ± 0.40 [35]
A(2001)	2050	9.76 ± 0.12	24.01 ± 2.26	0.013 ± 0.001	10.55 ± 0.12

n.a.—not applied.

Table 2 shows that for the OIHs A(270), A(400), A(403), A(600), A(900), and A(2000), as the molecular weight of the Jeffamines[®] used in the synthesis increases, the normalized resistance (R) decreases, which is in accordance with the literature [22,35]. The difference obtained for the resistance of A(270) compared to A(400) may be due to the fact that Jeffamine[®] RFD-270 is an aliphatic amine containing both rigid (cycloaliphatic) and flexible (etheramine) segments in the same molecule (vide Figure 1). In the case of A(400), the Jeffamine[®] used in the synthesis (Jeffamine[®] D-400) is a difunctional primary amine. This polyetheramine is characterized by repeating oxypropylene units in the backbone. This difference between the backbones of the Jeffamines[®] used (i.e., RFD-270 and D-400) may explain the two orders of magnitude difference found between the resistance of A(270) and A(400) and the capacitance that in case of A(400) is 4.375 times higher than A(270). Regarding the A(170) samples, a lower resistance was expected considering the molecular weight of the Jeffamine[®] used (1700 g mol^{-1}). Previous publications showed that as the molecular weight of the Jeffamine[®] increases, the resistance of the OIHs decreases due to the organic component increase [22,35]. Jeffamine[®] THF-170 is chemically based on a [poly(tetramethylene ether glycol)]/(poly(propylene glycol)) copolymer that contains a significant amount of secondary as well as primary amines. Therefore, this might be the main reason for the high resistance obtained. The main difference between the resistance obtained for A(2000) and A(2001) can be explained by the disparity between the Jeffamine[®] used in each synthesis. A(2001) was synthesized using a difunctional secondary amine (Jeffamine[®] SD-2001) while A(2000) was obtained using a polyether diamine based predominantly on a polyethylene glycol (PEG) backbone. Jeffamine[®] SD-2001 is a difunctional secondary amine derived from the Jeffamine[®] D-2000 amine, which are polyether diamines based on a poly(propylene glycol) (PPG) backbone. This may explain

the main differences found between A(2000) and A(2001) regarding the electrical properties (Table 2) in which the resistance of A(2001) increases 2.04 times compared to the resistance obtained for A(2000).

The new OIH materials synthesized show a ϵ_r between 8 and 24, with A(170) and A(2001) showing the lowest and the highest values, respectively. The capacitance values obtained are between 0.008 and 0.013 nF cm⁻², with A(170) and A(2001) showing the lowest and the highest, respectively. Moreover, the new amino-alcohol-based sol-gel materials show lower ϵ_r and capacitance values than the ones already reported.

3.4. Preliminary Assessment of the OIH in Contact with Cement Paste

A preliminary assessment of the OIH materials in contact with a cement paste prepared with a w/c = 0.5 was conducted. The preliminary tests were only performed for the OIHs with the highest transmittance values, i.e., A(403), A(270), and A(170). The main objective of these studies was to assess if these new OIHs were stable and resistant when in contact with a high alkaline environment. A cement paste with a w/c = 0.5 was chosen to mimic the concrete alkalinity. The samples were immersed in the cement paste for 7, 14, and for 28 days. After 7, 14, and 28 days the cured paste samples were broken to check the physical aspect of the samples. Figure 7 shows the samples A(270), A(403), and A(170) after 7 days of being embedded in the mentioned cement paste.

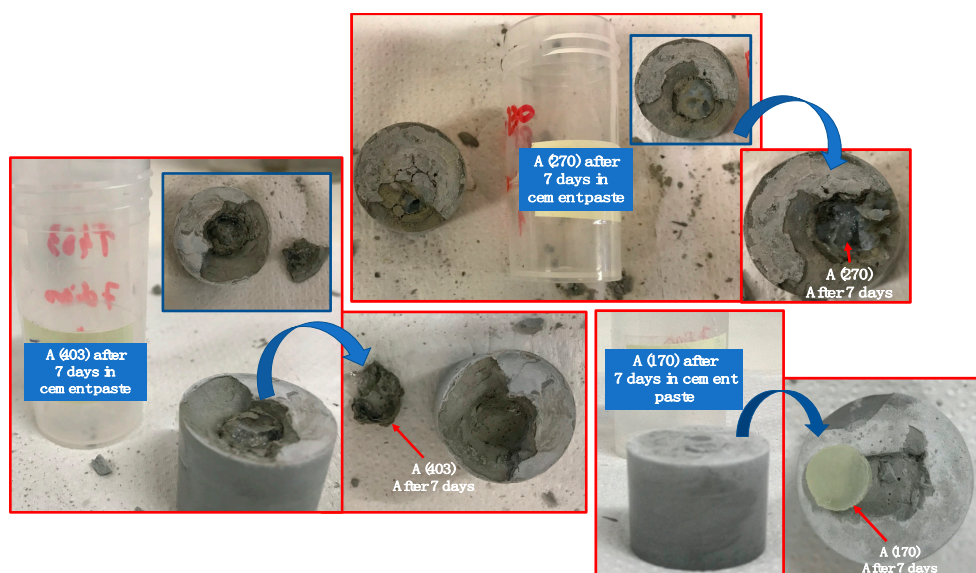


Figure 7. OIH samples (A(270), A(403), and A(170)) after 7 days immersed in cement paste with a w/c = 0.5.

Figure 8 shows the results obtained for the OIH samples after 28 days of being embedded in the cement paste.

After 7 days of contact with the cement paste (Figure 7), except for OIH sample A(170), OIH A(270) and A(403) suffered severe degradation and reacted with the cement paste. Even though sample A(403) seems to be less resistant than A(270), due to the alkalinity of the cement pastes, it was not possible to extract OIH samples A(270) and A(403) from the cement paste after 7 days, as can be observed in Figure 7. Sample A(170) appears to be resistant to the high alkaline environment of the cement paste and did not experience visible degradation. It can be observed that after 28 days the same behavior was found. OIH sample A(170) showed improved stability when compared to the other samples. The promising preliminary results suggest that further tests such as EIS should be conducted. By performing EIS measurements, i.e., assessing resistance and capacitance of the A(170) samples before and after immersion in the cement pastes, it will be possible to quantify the degradation impact of the alkaline environment.

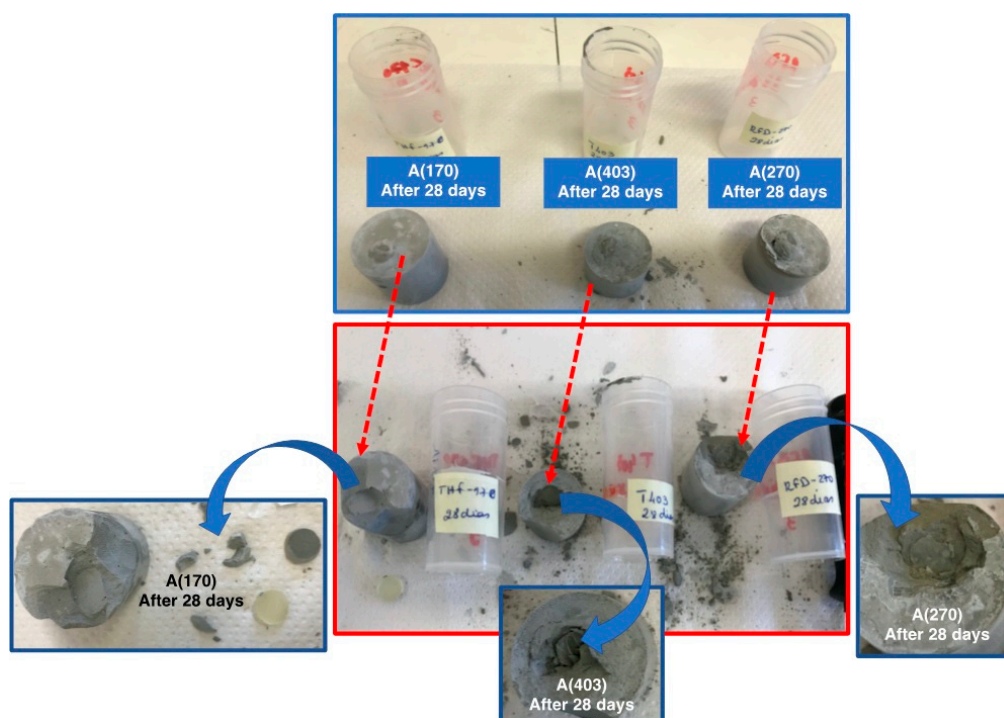


Figure 8. OIH samples (A(270), A(403), and A(170)) after 28 days immersed in cement paste with a w/c = 0.5.

Considering the results obtained, the thickness of the OIH A(170) films was measured before and after 7, 14, and 28 days of being embedded in the cement paste. Table 3 shows the thicknesses obtained for each A(170) OIH film tested.

Table 3. Thickness of the OIH films measured after 7, 14, and 28 days embedded in cement paste with a w/c = 0.5.

OIH Sample	Thickness/mm			
	Before Exposure to Cement Paste	After 7 Days in Cement Paste	After 14 Days in Cement Paste	After 28 Days in Cement Paste
A(170)	1.387	1.343 ($\Delta = 0.044$)	1.472 ($\Delta = 0.019$)	1.798 ($\Delta = 0.004$)
	1.491			
	1.802			

Table 3 shows that thickness decreases slightly over time for the A(170) samples. After 28 days a decrease of 0.22% of thickness was found. The highest decrease percentage was found for the OIH sample exposed for 7 days (around 3.17%), followed by the sample exposed for 14 days, which lost around 1.27% thickness.

4. Conclusions

The synthesis of the five new OIH sol-gel materials, homogeneous and crack-free, based on amino-alcohol silicate matrices, namely A(148), A(270), A(403), A(170), and A(2001), has been reported. The results obtained allow for the conclusion that the different Jeffamines[®] used influence the optical and the electrochemical properties. The OIH matrices with the lowest and highest transmittance, between 400 and 700 nm, were given by A(2001) and A(403), respectively. The photoluminescence spectra obtained for xerogel films A(148), A(270), A(403), and A(170) allow for the conclusion that these materials show an intrinsic emission and provide generally shorter polyether chains than samples with higher photoluminescence. The capacitance values obtained were lower than the ones already reported

for similar materials and ranged between 0.008 and 0.013 nF cm⁻². The A(170) samples showed good behavior in contact with cement paste, allowing for the conclusion that only A(170) samples are resistant to highly alkaline environments. Therefore, considering the optical and electrical properties and the chemical stability of A(170) samples in contact with cement paste, it can be concluded that these samples show promising properties as support films in optical sensor fields such as fiber sensor devices for application in the civil engineering field. Regarding the A(270) and A(403) samples, it can be concluded that, despite the interesting optical and electrical properties, these OIH samples are not suitable to be used in highly alkaline environments. Moreover, further studies should be conducted on the A(170) samples in order to quantify the degradation impact due to the alkaline environment.

Author Contributions: Conceptualization, R.B.F. and C.J.R.S.; formal analysis, R.B.F, B.R.G., S.P.G.C., C.J.R.S., and M.M.M.R; funding acquisition, R.B.F. and C.J.R.S.; investigation, R.B.F. and B.R.G.; methodology, R.B.F. and C.J.R.S.; writing—original draft preparation, R.B.F.; writing—review and editing, R.B.F, B.R.G., S.P.G.C., C.J.R.S., and M.M.M.R.; project administration, R.B.F. and C.J.R.S.; resources, C.J.R.S. and R.B.F.; supervision, R.B.F. All authors have read and agreed to the published version of the manuscript with the exception of C.J.R.S.

Funding: This research was funded by the “SolSensors—Development of Advanced Fiber Optic Sensors for Monitoring the Durability of Concrete Structures” project, with the Program Budget COMPETE—Operational Program Competitiveness and Internationalization—COMPETE 2020 reference and the Lisbon Regional Operational Program (its FEDER component).

Acknowledgments: The authors acknowledge the reviewers for the constructive comments and suggestions and the support of Centro de Química, CQUM, which is financed by national funds through the FCT Foundation for Science and Technology, I.P. under project UID/QUI/00686/2020.

Conflicts of Interest: The authors declare no conflict of interest. The funders had no role in the design of the study; in the collection, analyses, or interpretation of data; in the writing of the manuscript, or in the decision to publish the results.

References

1. Bekiari, V.; Lianos, P. Tunable Photoluminescence from a Material Made by the Interaction between (3-Aminopropyl)triethoxysilane and Organic Acids. *Chem. Mater.* **1998**, *10*, 3777–3779. [[CrossRef](#)]
2. Carlos, L.D.; de Zea Bermudez, V.; Sá Ferreira, R.A.; Marques, L.; Assunção, M. Sol–Gel Derived Urea Cross-Linked Organically Modified Silicates. 2. Blue-Light Emission. *Chem. Mater.* **1999**, *11*, 581–588. [[CrossRef](#)]
3. Bekiari, V.; Lianos, P. Multicolor emission from terpyridine–lanthanide ion complexes encapsulated in nanocomposite silica/poly(ethylene glycol) sol–gel matrices. *J. Lumin.* **2003**, *101*, 135–140. [[CrossRef](#)]
4. Kober, U.A.; Gallas, M.R.; Campo, L.F.; Rodembusch, F.S.; Stefani, V. Fluorescence emission modulation in singlefluoroforic submicro-sized silica particles. *J. Sol-Gel Sci. Technol.* **2009**, *52*, 305–308. [[CrossRef](#)]
5. Pletsch, D.; da Santos, F.S.; Severo Rodembusch, F.; Stefani, V.; Franciscato Campo, L. Bis-silylated terephthalate as a building block precursor for highly fluorescent organic–inorganic hybrid materials. *New J. Chem.* **2012**, *36*, 2506–2513. [[CrossRef](#)]
6. Ribeiro, S.J.L.; Dahmouche, K.; Ribeiro, C.A.; Santilli, C.V.; Pulcinelli, S.H. Study of Hybrid Silica-Polyethyleneglycol Xerogels by Eu³⁺ Luminescence Spectroscopy. *J. Sol-Gel Sci. Technol.* **1998**, *13*, 427–432. [[CrossRef](#)]
7. Bekiari, V.; Lianos, P.; Judeinstein, P. Efficient luminescent materials made by incorporation of terbium(III) and 2,2-bipyridine in silica/poly(ethylene oxide) hybrid gels. *Chem. Phys. Lett.* **1999**, *307*, 310–316. [[CrossRef](#)]
8. Severo Rodembusch, F.; Franciscato Campo, L.; Stefani, V.; Rigacci, A. The first silica aerogels fluorescent by excited state intramolecular proton transfer mechanism (ESIPT). *J. Mater. Chem.* **2005**, *15*, 1537–1541. [[CrossRef](#)]
9. Grando, S.R.; Pessoa, C.M.; Gallas, M.R.; Costa, T.M.H.; Rodembusch, F.S.; Benvenuto, E.V. Modulation of the ESIPT Emission of Benzothiazole Type Dye Incorporated in Silica-Based Hybrid Materials. *Langmuir* **2009**, *25*, 13219–13223. [[CrossRef](#)]
10. Barja, B.C.; Bari, S.E.; Marchi, M.C.; Iglesias, F.L.; Bernardi, M. Luminescent Eu(III) hybrid sensors for in situ copper detection. *Sens. Actuators B Chem.* **2011**, *158*, 214–222. [[CrossRef](#)]

11. Nolasco, M.M.; Vaz, P.M.; Freitas, V.T.; Lima, P.P.; André, P.S.; Ferreira, R.A.S.; Vaz, P.D.; Ribeiro-Claro, P.; Carlos, L.D. Engineering highly efficient Eu(III)-based tri-ureasil hybrids toward luminescent solar concentrators. *J. Mater. Chem. A* **2013**, *1*, 7339–7350. [[CrossRef](#)]
12. Brito, J.B.; Costa, T.M.H.; Rodembusch, F.S.; Konowalow, A.S.; dos Reis, R.M.S.; Balzaretto, N.M.; da Jornada, J.A.H. Blue–green luminescent carbon nanodots produced in a silica matrix. *Carbon* **2015**, *91*, 234–240. [[CrossRef](#)]
13. He, W.; Xie, Y.; Xing, Q.; Ni, P.; Han, Y.; Dai, H. Sol-gel synthesis of biocompatible Eu³⁺/Gd³⁺ co-doped calcium phosphate nanocrystals for cell bioimaging. *J. Lumin.* **2017**, *192*, 902–909. [[CrossRef](#)]
14. de Zea Bermudez, V.; Carlos, L.D.; Alcácer, L. Sol–Gel Derived Urea Cross-Linked Organically Modified Silicates. 1. Room Temperature Mid-Infrared Spectra. *Chem. Mater.* **1999**, *11*, 569–580. [[CrossRef](#)]
15. Boev, V.I.; Soloviev, A.; Silva, C.J.R.; Gomes, M.J.M.; Barber, D.J. Highly transparent sol-gel derived ureasilicate monoliths exhibiting long-term optical stability. *J. Sol-Gel Sci. Technol.* **2006**, *41*, 223–229. [[CrossRef](#)]
16. Boev, V.I.; Soloviev, A.; Silva, C.J.R.; Gomes, M.J.M. Incorporation of CdS nanoparticles from colloidal solution into optically clear ureasilicate matrix with preservation of quantum size effect. *Solid State Sci.* **2006**, *8*, 50–58. [[CrossRef](#)]
17. Gonçalves, L.F.F.F.; Silva, C.J.R.; Kanodarwala, F.K.; Stride, J.A.; Pereira, M.R.; Gomes, M.J.M. Synthesis and characterization of organic–inorganic hybrid materials prepared by sol–gel and containing Zn_xCd_{1–x}S nanoparticles prepared by a colloidal method. *J. Lumin.* **2013**, *144*, 203–211. [[CrossRef](#)]
18. Moreira, S.D.F.C.; Silva, C.J.R.; Prado, L.A.S.A.; Costa, M.F.M.; Boev, V.I.; Martín-Sánchez, J.; Gomes, M.J.M. Development of new high transparent hybrid organic-inorganic monoliths with surface engraved diffraction pattern. *J. Polym. Sci. Part B Polym. Phys.* **2012**, *50*, 492–499. [[CrossRef](#)]
19. Figueira, R.B.; Silva, C.J.; Pereira, E.V.; Salta, M.M. Ureasilicate Hybrid Coatings for Corrosion Protection of Galvanized Steel in Cementitious Media. *J. Electrochem. Soc.* **2013**, *160*, C467–C479. [[CrossRef](#)]
20. Gonçalves, L.F.F.F.; Silva, C.J.R.; Kanodarwala, F.K.; Stride, J.A.; Pereira, M.R.; Gomes, M.J.M. Synthesis of an optically clear, flexible and stable hybrid ureasilicate matrix doped with CdSe nanoparticles produced by reverse micelles. *Mater. Chem. Phys.* **2014**, *147*, 86–94. [[CrossRef](#)]
21. Molina, E.F.; Parreira, R.L.T.; De Faria, E.H.; de Carvalho, H.W.P.; Caramori, G.F.; Coimbra, D.F.; Nassar, E.J.; Ciuffi, K.J. Ureasil-Poly(ethylene oxide) Hybrid Matrix for Selective Adsorption and Separation of Dyes from Water. *Langmuir* **2014**, *30*, 3857–3868. [[CrossRef](#)] [[PubMed](#)]
22. Figueira, R.B.; Silva, C.J.R.; Pereira, E.V. Hybrid sol–gel coatings for corrosion protection of hot-dip galvanized steel in alkaline medium. *Surf. Coat. Technol.* **2015**, *265*, 191–204. [[CrossRef](#)]
23. Correia, S.F.H.; Antunes, P.; Pecoraro, E.; Lima, P.P.; Varum, H.; Carlos, L.D.; Ferreira, R.A.S.; André, P.S. Optical Fiber Relative Humidity Sensor Based on a FBG with a Di-Ureasil Coating. *Sensors* **2012**, *12*, 8847–8860. [[CrossRef](#)] [[PubMed](#)]
24. de Jesus, N.A.M.; de Oliveira, A.H.P.; Tavares, D.C.; Furtado, R.A.; de Silva, M.L.A.; Cunha, W.R.; Molina, E.F. Biofilm formed from a tri-ureasil organic–inorganic hybrid gel for use as a cubein release system. *J. Sol-Gel Sci. Technol.* **2018**, *88*, 192–201. [[CrossRef](#)]
25. Nunes, S.C.; Fernandes, M.; Gonçalves, H.M.R.; Serrano, J.L.; Almeida, P.; de Bermudez, V.Z. Di-urea cross-linked siloxane hybrid materials incorporating oligo(oxypropylene) and oligo(oxyethylene) chains. *J. Sol-Gel Sci. Technol.* **2020**, 1–15. [[CrossRef](#)]
26. Gonçalves, L.F.F.F.; Kanodarwala, F.K.; Stride, J.A.; Silva, C.J.R.; Gomes, M.J.M. One-pot synthesis of CdS nanoparticles exhibiting quantum size effect prepared within a sol–gel derived ureasilicate matrix. *Opt. Mater.* **2013**, *36*, 186–190. [[CrossRef](#)]
27. Gonçalves, L.F.F.F.; Silva, C.J.R.; Kanodarwala, F.K.; Stride, J.A.; Gomes, M.J.M. Synthesis and characterization of organic–inorganic hybrid materials prepared by sol–gel and containing CdS nanoparticles prepared by a colloidal method using poly(*N*-vinyl-2-pyrrolidone). *J. Sol-Gel Sci. Technol.* **2014**, *71*, 69–78. [[CrossRef](#)]
28. Gonçalves, L.F.F.F.; Silva, C.J.R.; Kanodarwala, F.K.; Stride, J.A.; Pereira, M.R.; Gomes, M.J.M. Influence of Cd²⁺/S^{2–} molar ratio and of different capping environments in the optical properties of CdS nanoparticles incorporated within a hybrid diureasil matrix. *Appl. Surf. Sci.* **2014**, *314*, 877–887. [[CrossRef](#)]
29. Gonçalves, L.F.F.F.; Kanodarwala, F.K.; Stride, J.A.; Silva, C.J.R.; Pereira, M.R.; Gomes, M.J.M. One-pot synthesis of CdSe nanoparticles exhibiting quantum size effect within a sol–gel derived ureasilicate matrix. *J. Photochem. Photobiol. Chem.* **2014**, *285*, 21–29. [[CrossRef](#)]

30. Gonçalves, J.T.; Boev, V.I.; Solovyev, A.; Silva, C.J.R.; Gomes, M.J.M. Luminescence and Absorption of Hybrid Xerogels Doped with PbS Nanoparticles Prepared by Gas Diffusion Method. *Mater. Sci. Forum* **2006**, *514–516*, 1221–1224. [[CrossRef](#)]
31. Figueira, R.B.; Silva, C.J.R.; Pereira, E.V. Influence of Experimental Parameters Using the Dip-Coating Method on the Barrier Performance of Hybrid Sol-Gel Coatings in Strong Alkaline Environments. *Coatings* **2015**, *5*, 124–141. [[CrossRef](#)]
32. Figueira, R.B.; Silva, C.J.; Pereira, E.V. Ureasilicate Hybrid Coatings for Corrosion Protection of Galvanized Steel in Chloride-Contaminated Simulated Concrete Pore Solution. *J. Electrochem. Soc.* **2015**, *162*, C666–C676. [[CrossRef](#)]
33. Figueira, R.B.; Callone, E.; Silva, C.J.R.; Pereira, E.V.; Dirè, S. Hybrid Coatings Enriched with Tetraethoxysilane for Corrosion Mitigation of Hot-Dip Galvanized Steel in Chloride Contaminated Simulated Concrete Pore Solutions. *Materials* **2017**, *10*, 306. [[CrossRef](#)] [[PubMed](#)]
34. Willis-Fox, N.; Kraft, M.; Arlt, J.; Scherf, U.; Evans, R.C. Tunable White-Light Emission from Conjugated Polymer-Di-Ureasil Materials. *Adv. Funct. Mater.* **2016**, *26*, 532–542. [[CrossRef](#)]
35. Figueira, R.B.; Silva, C.J.; Pereira, E.V.; Salta, M.M. Alcohol-Aminosilicate Hybrid Coatings for Corrosion Protection of Galvanized Steel in Mortar. *J. Electrochem. Soc.* **2014**, *161*, C349–C362. [[CrossRef](#)]
36. Cho, N.; Kim, N.; Jang, J.; Chang, S. Estimation of deflection curve of bridges using fiber optic strain sensors. In Proceedings of the Smart Structures and Materials 2000: Smart Systems for Bridges, Structures, and Highways; International Society for Optics and Photonics, Newport Beach, CA, USA, 6 March 2000; SPIE: Bellingham, WA, USA, 2000; Volume 3988, pp. 339–348.
37. Kim, N.-S.; Cho, N.-S. Estimating deflection of a simple beam model using fiber optic bragg-grating sensors. *Exp. Mech.* **2004**, *44*, 433–439. [[CrossRef](#)]
38. Yehia, S.; Landolsi, T.; Hassan, M.; Hallal, M. Monitoring of strain induced by heat of hydration, cyclic and dynamic loads in concrete structures using fiber-optics sensors. *Measurement* **2014**, *52*, 33–46. [[CrossRef](#)]
39. Marković, M.Z.; Bajić, J.S.; Batilović, M.; Sušić, Z.; Joža, A.; Stojanović, G.M. Comparative Analysis of Deformation Determination by Applying Fiber-optic 2D Deflection Sensors and Geodetic Measurements. *Sensors* **2019**, *19*, 844. [[CrossRef](#)]
40. Wan, K.T.; Leung, C.K.Y. Applications of a distributed fiber optic crack sensor for concrete structures. *Sens. Actuators Phys.* **2007**, *135*, 458–464. [[CrossRef](#)]
41. Bao, T.; Wang, J.; Yao, Y. A fiber optic sensor for detecting and monitoring cracks in concrete structures. *Sci. China Technol. Sci.* **2010**, *53*, 3045–3050. [[CrossRef](#)]
42. Luo, D.; Yue, Y.; Li, P.; Ma, J.; Zhang, L.L.; Ibrahim, Z.; Ismail, Z. Concrete beam crack detection using tapered polymer optical fiber sensors. *Measurement* **2016**, *88*, 96–103. [[CrossRef](#)]
43. Baccay, M.A.; Otsuki, N.; Nishida, T.; Maruyama, S. Influence of Cement Type and Temperature on the Rate of Corrosion of Steel in Concrete Exposed to Carbonation. *Corrosion* **2006**, *62*, 811–821. [[CrossRef](#)]
44. Blanc, P.h.; Bourbon, X.; Lassin, A.; Gaucher, E.C. Chemical model for cement-based materials: Temperature dependence of thermodynamic functions for nanocrystalline and crystalline C–S–H phases. *Cem. Concr. Res.* **2010**, *40*, 851–866. [[CrossRef](#)]
45. Behnood, A.; Van Tittelboom, K.; De Belie, N. Methods for measuring pH in concrete: A review. *Constr. Build. Mater.* **2016**, *105*, 176–188. [[CrossRef](#)]
46. Plusquellec, G.; Geiker, M.R.; Lindgård, J.; Duchesne, J.; Fournier, B.; De Weerd, K. Determination of the pH and the free alkali metal content in the pore solution of concrete: Review and experimental comparison. *Cem. Concr. Res.* **2017**, *96*, 13–26. [[CrossRef](#)]
47. Wei, Y.; Guo, W.; Zheng, X. Integrated shrinkage, relative humidity, strength development, and cracking potential of internally cured concrete exposed to different drying conditions. *Dry. Technol.* **2016**, *34*, 741–752. [[CrossRef](#)]
48. Multon, S.; Toutlemonde, F. Effect of moisture conditions and transfers on alkali silica reaction damaged structures. *Cem. Concr. Res.* **2010**, *40*, 924–934. [[CrossRef](#)]
49. Zhang, W.; Min, H.; Gu, X. Temperature response and moisture transport in damaged concrete under an atmospheric environment. *Constr. Build. Mater.* **2016**, *123*, 290–299. [[CrossRef](#)]
50. Figueira, R.B.; Sadvovski, A.; Melo, A.P.; Pereira, E.V. Chloride threshold value to initiate reinforcement corrosion in simulated concrete pore solutions: The influence of surface finishing and pH. *Constr. Build. Mater.* **2017**, *141*, 183–200. [[CrossRef](#)]

51. Alonso, C.; Andrade, C.; Castellote, M.; Castro, P. Chloride threshold values to depassivate reinforcing bars embedded in a standardized OPC mortar. *Cem. Concr. Res.* **2000**, *30*, 1047–1055. [[CrossRef](#)]
52. Angst, U.; Elsener, B.; Larsen, C.K.; Vennesland, Ø. Critical chloride content in reinforced concrete—A review. *Cem. Concr. Res.* **2009**, *39*, 1122–1138. [[CrossRef](#)]
53. Figueira, R.B.; Sousa, R.; Coelho, L.; Azenha, M.; de Almeida, J.M.; Jorge, P.A.S.; Silva, C.J.R. Alkali-silica reaction in concrete: Mechanisms, mitigation and test methods. *Constr. Build. Mater.* **2019**, *222*, 903–931. [[CrossRef](#)]
54. Figueira, R.B. Electrochemical Sensors for Monitoring the Corrosion Conditions of Reinforced Concrete Structures: A Review. *Appl. Sci.* **2017**, *7*, 1157. [[CrossRef](#)]
55. Špírková, M.; Brus, J.; Hlavatá, D.; Kamisová, H.; Matejka, L.; Strachota, A. Preparation and characterisation of hybrid organic/inorganic coatings and films. *Surf. Coat. Int. Part B Coat. Trans.* **2003**, *86*, 187–193. [[CrossRef](#)]
56. Špírková, M.; Brus, J.; Hlavatá, D.; Kamišová, H.; Matějka, L.; Strachota, A. Preparation and characterization of hybrid organic–inorganic epoxide-based films and coatings prepared by the sol–gel process. *J. Appl. Polym. Sci.* **2004**, *92*, 937–950. [[CrossRef](#)]
57. Simcha, S.; Dotan, A.; Kenig, S.; Dodiuk, H. Characterization of Hybrid Epoxy Nanocomposites. *Nanomaterials* **2012**, *2*, 348–365. [[CrossRef](#)]
58. Alhwaige, A.A.; Alhassan, S.M.; Katsiotis, M.S.; Ishida, H.; Qutubuddin, S. Interactions, morphology and thermal stability of graphene-oxide reinforced polymer aerogels derived from star-like telechelic aldehyde-terminal benzoxazine resin. *RSC Adv.* **2015**, *5*, 92719–92731. [[CrossRef](#)]
59. Meazzini, I.; Willis-Fox, N.; Blayo, C.; Arlt, J.; Clément, S.; Evans, R.C. Targeted design leads to tunable photoluminescence from perylene dicarboxydiimide–poly(oxyalkylene)/siloxane hybrids for luminescent solar concentrators. *J. Mater. Chem. C* **2016**, *4*, 4049–4059. [[CrossRef](#)]
60. Erdem, A.; Ngwabebhoh, F.A.; Yildiz, U. Synthesis, characterization and swelling investigations of novel polyetheramine-based hydrogels. *Polym. Bull.* **2017**, *74*, 873–893. [[CrossRef](#)]
61. Carlos, L.D.; Sá Ferreira, R.A.; Pereira, R.N.; Assunção, M.; de Zea Bermudez, V. White-Light Emission of Amine-Functionalized Organic/Inorganic Hybrids: Emitting Centers and Recombination Mechanisms. *J. Phys. Chem. B* **2004**, *108*, 14924–14932. [[CrossRef](#)]
62. Bekiari, V.; Lianos, P.; Stangar, U.L.; Orel, B.; Judeinstein, P. Optimization of the Intensity of Luminescence Emission from Silica/Poly(ethylene oxide) and Silica/Poly(propylene oxide) Nanocomposite Gels. *Chem. Mater.* **2000**, *12*, 3095–3099. [[CrossRef](#)]
63. Cordoncillo, E.; Guaita, F.J.; Escribano, P.; Philippe, C.; Viana, B.; Sanchez, C. Blue emitting hybrid organic–inorganic materials. *Opt. Mater.* **2001**, *18*, 309–320. [[CrossRef](#)]
64. Santos, T.C.F.; Rodrigues, R.R.; Correia, S.F.H.; Carlos, L.D.; Ferreira, R.A.S.; Molina, C.; Péres, L.O. UV-converting blue-emitting polyfluorene-based organic-inorganic hybrids for solid state lighting. *Polymer* **2019**, *174*, 109–113. [[CrossRef](#)]
65. Yasakau, K.A.; Ferreira, M.G.S.; Zheludkevich, M.L. Sol-Gel Coatings with Nanocontainers of Corrosion Inhibitors for Active Corrosion Protection of Metallic Materials. In *Handbook of Sol-Gel Science and Technology*; Klein, L., Aparicio, M., Jitianu, A., Eds.; Springer International Publishing: Berlin, Germany, 2017; pp. 1–37, ISBN 978-3-319-19454-7.
66. Orazem, M.E.; Tribollet, B. *Electrochemical Impedance Spectroscopy*; Wiley: Hoboken, NJ, USA, 2008; ISBN 978-0-470-38157-1.
67. Barsoukov, E.; Macdonald, J.R. Impedance spectroscopy: Theory, experiment, and applications. *History* **2005**, *1*, 1–13.
68. Zoltowski, P. On the electrical capacitance of interfaces exhibiting constant phase element behaviour. *J. Electroanal. Chem.* **1998**, *443*, 149–154. [[CrossRef](#)]

Publisher’s Note: MDPI stays neutral with regard to jurisdictional claims in published maps and institutional affiliations.



© 2020 by the authors. Licensee MDPI, Basel, Switzerland. This article is an open access article distributed under the terms and conditions of the Creative Commons Attribution (CC BY) license (<http://creativecommons.org/licenses/by/4.0/>).